

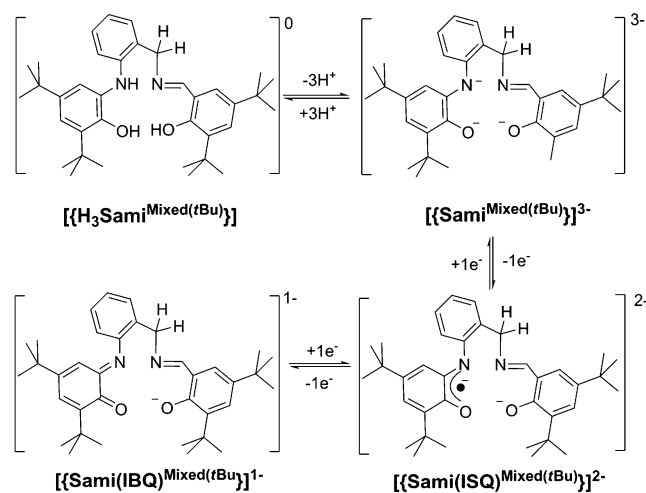
Figure 1. (Top) Orthogonal and nonorthogonal arrangement between Cu(II) $d_{x^2-y^2}$ and π -radical p_z orbitals; (middle) twist angle between biting planes; (bottom) dihedral angle between the Cu(II)-coordination plane and the phenyl ring.

Cu(II) complexes has been argued as the deciding factor for the ferromagnetic (orthogonal arrangement between the interacting magnetic orbitals, Figure 1) and antiferromagnetic (nonorthogonal arrangement between the interacting magnetic orbitals, Figure 1) couplings between the Cu(II) center and the coordinated π -radical center.⁸ While the variation in the dihedral angle (Figure 1), which is defined as the twist angle between the radical-containing phenyl plane and the Cu(II)-centric coordination plane that formed by four coordinating atoms, has also been demonstrated as the major factor for the diversity in coupling fashions.^{3d,7d,9} Hence, an attempt has been taken to identify the predominating factor, i.e., tetrahedral distortion vs dihedral angle for assigning the coupling fashion.

Cu(II) complexes synthesized using salen-type ligands are known to acquire nonplanar geometry around the Cu(II) center,¹⁰ while noninnocent ligands upon coordination with the Cu(II) ion under air provide π -radical-coordinated Cu(II) complexes. Hence, a combination of both the salen unit and the noninnocent unit in a single ligand will provide a π -radical-containing Cu(II) complex with a distorted coordination environment around the Cu(II) center. Consequently, the effect of distortion in a stable π -radical-coordinated Cu(II) complex could be examined. Furthermore, the nuclearity of the resulting Cu(II) complex could be restricted to one by keeping the donor (capable of coordinating) atoms per coordinating ligand to four. Hence, a mononuclear π -radical-coordinated Cu(II) complex will result. In this regard, a tetradentate ligand, which will be noted here as $\text{H}_3\text{Sami}^{\text{Mixed}(\text{tBu})}$, was designed (Scheme 1). The ligand was comprised of two compartments, a redox-active noninnocent 2-aminophenol and a salen salicylidene, which are bridged by a benzyl linker.

Herein, the synthesis and characterization of a monoradical-containing Cu(II) complex (complex 1) formed with ligand $\text{H}_3\text{Sami}^{\text{Mixed}(\text{tBu})}$ are discussed. Interestingly, it had been observed that complex 1 in solution (CH_2Cl_2) under air experienced ligand-centered oxidation at the benzyl position. Thus, formed complex (complex 2) has also been characterized. The structural difference between complex 1 and

Scheme 1. Schematic Representation of Ligand $\text{H}_3\text{Sami}^{\text{Mixed}(\text{tBu})}$ and the Possible Different Redox States^a



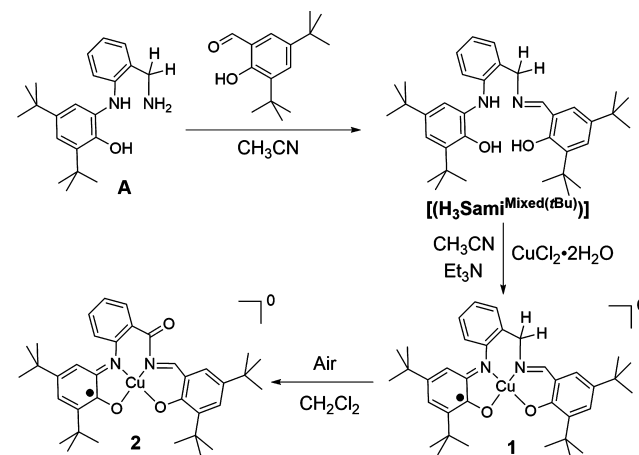
^aISQ and IBQ stand for the iminobenzosemiquinone and iminobenzoquinone forms of the ligand, respectively.

complex 2 and its influence to the corresponding electronic structure, including magnetic coupling fashion, have been investigated. DFT and TD-DFT calculations were also performed for better realization of the geometrical influences to the electronic structures and are presented here.

RESULTS AND DISCUSSION

A schematic diagram for the synthesis of complexes 1 and 2 is shown in Scheme 2. Ligand $\text{H}_3\text{Sami}^{\text{Mixed}(\text{tBu})}$ was generated in

Scheme 2. Schematic Representation of the Ligand and the Corresponding Cu(II) Complexes Formation Route



situ by reacting 1:1 A and 3,5-di-tert-butylsalicylaldehyde in CH_3CN under refluxing condition. Addition of $\text{CuCl}_2 \cdot 2\text{H}_2\text{O}$ to the in-situ-generated ligand $\text{H}_3\text{Sami}^{\text{Mixed}(\text{tBu})}$ in the presence of Et_3N provided complex 1 in 50% yield. The complex was stable under air in the solid state. However, it changed gradually to complex 2 (Scheme 2) in solution in 20% yield in a 5 day time span. Due to the sluggish nature of the conversion, identification of the intermediate/s for the process was not possible.

In the infrared spectra of 1 and 2, asymmetric, overtone, and symmetric $\nu(\text{C}-\text{H})$ stretches for the *tert*-butyl groups appeared

nearly in the same region at 2960, 2906, and 2872 cm^{-1} , respectively. Complexes **1** and **2** showed the characteristic $\nu(\text{C}=\text{N})$ stretch at 1619 and 1621 cm^{-1} , respectively. In addition, a band appeared at 1657 cm^{-1} in the infrared spectrum of **2**, indicating the presence of a conjugated keto functional group (amide unit) in the coordinating ligand unit.

The electrospray ionization mass (ESI-MS) spectra of $\text{H}_3\text{Sami}^{\text{Mixed}(\text{tBu})}$, **1**, and **2** species were measured in positive-ion mode in CH_3CN solution. The in-situ-generated ligand $\text{H}_3\text{Sami}^{\text{Mixed}(\text{tBu})}$ showed a 100% peak at $m/z = 543.31$ $\{[\text{M} + \text{H}]^+\}$, and the simulation of the isotope distribution pattern confirmed the formation of the expected ligand with $\text{C}_{36}\text{H}_{50}\text{N}_2\text{O}_2$ composition. The peaks at $m/z = 602.53$ $([\text{C}_{36}\text{H}_{47}\text{CuN}_2\text{O}_2]^+)$ indicated the formation of **1** by incorporation of a copper atom to $[\text{Sami}^{\text{Mixed}(\text{tBu})}]^{n-}$. The crystalline solid isolated after conversion of **1** to **2** has shown a 100% $[\text{M}]^+$ mass peak at $m/z = 616.54$ from the ESI-MS spectrum. The isotope distribution pattern revealed the $\text{C}_{36}\text{H}_{45}\text{CuN}_2\text{O}_3$ composition for **2**.

Single-crystal X-ray diffraction measurements for complexes **1** and **2** were performed at 296(2) K. Complex **1** crystallized in the monoclinic space group $C12/c1$, while complex **2** crystallized in the orthorhombic space group $P2_12_12_1$. Single-crystal X-ray molecular structures of complexes **1** and **2** are shown in Figure 2. Selected bond distances and bond angles are presented in Table 1.

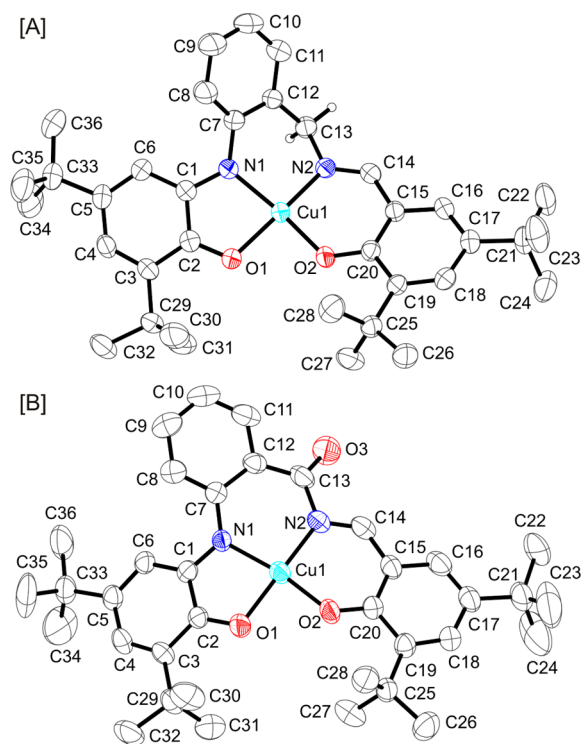


Figure 2. ORTEP plots of the molecular structures of complexes **1** (A) and **2** (B). Hydrogen atoms are omitted for clarity.

From the molecular structures of complexes **1** and **2** it was found that in both complexes the central Cu1 atom was surrounded by a N_2O_2 donor environment of the coordinated tetradentate ligand. The difference in the ligand backbone between complex **1** and complex **2** was only at C13 position: a benzyl group in **1** and a carbonyl group in **2**. While in both complexes Cu1–N1 and Cu1–N2 bond distances were almost

Table 1. Selected Bond Distances (Angstroms) and Bond Angles (degrees) for **1** and **2**

	1	2
Cu1–N1	1.9312(17)	1.934(4)
Cu1–N2	1.9205(17)	1.935(5)
Cu1–O1	1.9265(15)	1.928(4)
Cu1–O2	1.8577(14)	1.877(4)
C2–O1	1.289(2)	1.299(6)
C1–N1	1.354(2)	1.350(7)
C1–C2	1.443(3)	1.421(8)
C2–C3	1.438(3)	1.440(7)
C3–C4	1.360(3)	1.368(8)
C4–C5	1.423(3)	1.402(8)
C5–C6	1.363(3)	1.372(8)
C6–C1	1.419(3)	1.423(8)
N1–C7	1.404(3)	1.384(7)
C7–C8	1.399(3)	1.401(8)
C8–C9	1.378(3)	1.348(8)
C9–C10	1.380(3)	1.388(9)
C10–C11	1.386(3)	1.357(9)
C11–C12	1.385(3)	1.395(8)
C12–C7	1.404(3)	1.436(8)
C12–C13	1.510(3)	1.466(9)
C13–O3		1.212(7)
C13–N2	1.475(2)	1.425(7)
C20–O2	1.312(2)	1.281(6)
C14–N2	1.290(2)	1.307(7)
C14–C15	1.446(3)	1.414(8)
C15–C16	1.407(3)	1.422(8)
C16–C17	1.372(3)	1.373(9)
C17–C18	1.409(3)	1.400(8)
C18–C19	1.385(3)	1.358(8)
C19–C20	1.423(3)	1.454(8)
C20–C15	1.425(3)	1.426(8)
O1–Cu1–N1	83.25(7)	83.20(18)
N1–Cu1–N2	95.36(7)	95.3(2)
N2–Cu1–O2	94.21(7)	94.75(19)
O2–Cu1–O1	90.68(6)	87.17(17)
O1–Cu1–N2	163.85(7)	170.3(2)
N1–Cu1–O2	165.01(7)	169.72(18)
Cu1–O1–C2	113.17(14)	111.6(4)
Cu1–N1–C1	112.87(13)	110.6(4)
Cu1–N1–C7	122.87(14)	125.3(4)
Cu1–N2–C13	115.89(13)	125.0(4)
Cu1–N2–C14	124.63(15)	120.4(4)
Cu1–O2–C20	127.76(13)	128.9(4)

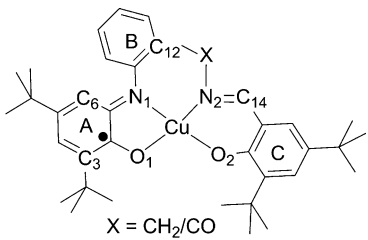
equal and in the range of 1.921–1.935 Å, a significant shortening in Cu1–O2 = 1.8577(14) [**1**] and 1.877(4) [**2**] Å compared to Cu1–O1 = 1.9265(15) [**1**] and 1.928(4) [**2**] Å was noticed. This deviation was because of the higher covalent character in the Cu1–O2 bond due to the fully reduced phenolate form of the coordinating O2 site, while the coordinating O1 atom was associated with the one-electron-oxidized iminobenzosemiquinone form of the 2-amidophenolate moiety (vide infra). However, the above-mentioned metal–ligand bond distances were in accord with the +II oxidation state of the central Cu1 atom.^{2e,11} The angles N1–Cu1–O2 and N2–Cu1–O1 were 165.01(7)° [**1**] and 169.72(18)° [**2**] and 163.85(7)° [**1**] and 170.30(20)° [**2**], respectively. These represented a slight deviation of the coordination geometry from square planar. The structural rhombic distortion

parameters, τ_4 ,¹² for complexes **1** and **2** were 0.22 and 0.14, respectively. These indicated that the deviation in the coordination environment from planar (square planar, $\tau_4 = 0$) to nonplanar (tetrahedral, $\tau_4 = 1$) geometry was more pronounced in **1** compared to **2**.

In the complexes all C–C bond distances in the C₆ aryl rings were not the same and not in the range of 1.39 ± 0.01 Å. Alternating short and long C–C bond distances, i.e., a quinoid-type distortion, was observed in the *tert*-butyl groups containing an amidophenolate unit in both complexes. The respective C1–C2, C2–C3, C3–C4, C4–C5, C5–C6, and C6–C1 bond distances were 1.443(3), 1.438(3), 1.360(3), 1.423(3), 1.363(3), and 1.419(3) Å for complex **1** and 1.421(8), 1.440(7), 1.368(8), 1.402(8), 1.372(8), and 1.423(8) Å for complex **2**. The C2–O1 and C1–N1 bond distances were 1.289(2) [1] and 1.299(6) [2] Å and 1.354(2) [1] and 1.350(7) [2] Å, respectively. These bond distances were neither in accord with their respective single-bond character nor commensurate with the double-bond character. Rather, the bonds were between single-bond and double-bond values. These bond distances along with the quinoid-type distortion emphasized the one-electron-oxidized iminobenzosemiquinone (ISQ^{•1-}) form of the coordinating amidophenolate units. Note, alternate short and long bond distances were also found in the salicylidene unit in both complexes because of delocalization of the phenolate¹⁻ charge from phenolate¹⁻ to the imine unit in complex **1** and phenolate¹⁻ to the C=O unit in complex **2**.¹³ This type of distortion in the salen unit is common in metal-salen complexes, where the salicylidene unit exists in the fully reduced form.¹⁴ Thus, the coordinated ligand overall acquired a dianionic charge (π -radical anion and phenolate anion) and provided the neutral Cu(II) complexes.

A detailed solid-state structural comparison between complex **1** and complex **2** was done, and the parameters are given in Table 2. The X = –CH₂ unit in **1** was sp³ hybridized. Therefore, the six-membered ring that formed by Cu–N1–C7–C12–C13–N2 atoms had a half-chair configuration and the X = –CH₂ unit was –0.81 Å below (negative sign indicates the below position, Figure 3C) the plane that was constituted

Table 2. Comparative Structural Parameters of **1** and **2**



parameters	1 (X = CH ₂)	2 (X = CO)
angle between plane A and plane B	44.42°	39.15°
angle between plane B and plane C	57.81°	19.10°
angle between plane A and plane C	25.41°	34.35°
distance of Cu(II) from plane A	–0.24 Å	–0.50 Å
distance of Cu(II) from plane C	+0.31 Å	–0.23 Å
distance of X from C12–N2–C14 plane	–0.81 Å	–0.17 Å
angle between N1–Cu–O1 and N2–Cu–O2 planes (twist angle)	20.65°	10.00°
angle between N1–Cu–O1 and A planes (bent angle)	8.81°	19.92°
torsion angle between N1–O1–C3–C6 atoms	3.60°	8.67°

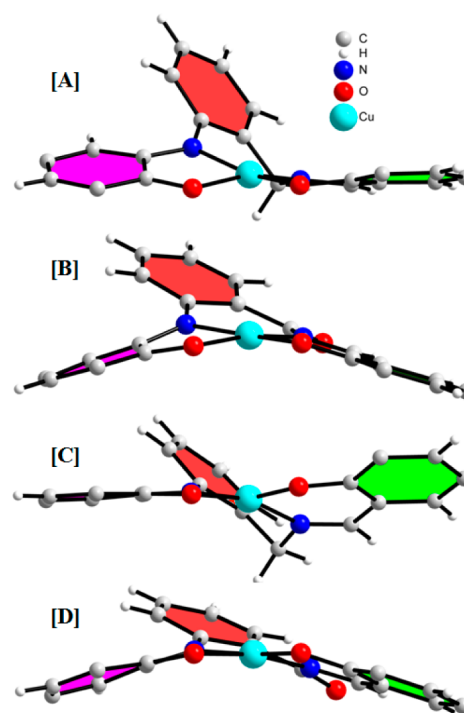


Figure 3. Perspective views of **1** (A and C) and **2** (B and D). *tert*-Butyl groups were omitted for clarity.

by C12–N2–C14 atoms. On oxidation of X = –CH₂ to X = –C=O (keto) the hybridization of X changed from sp³ to sp² and the X = –C=O unit came closer (–0.17 Å) to the plane. This change in hybridization caused significant lowering in the angle between B and C planes (Table 2) and the twist angle between N1–Cu–O1 and N2–Cu–O2 planes (Table 2, Figure 3). The Cu atom in complex **1** was found to situate below the plane A and above the plane C (Table 2), while the atom was situating below both planes in complex **2**. In complex **1**, the angle between A and C planes was 25.41° and the twist angle (Table 2) was 20.65°. This implied that the virtual angle between A and C planes was $25.41^\circ - 20.65^\circ = 4.76^\circ$; hence, the complex was more planar (Figure 3A) than complex **2**, which had a $34.35^\circ - 10.00^\circ = 24.35^\circ$ virtual angle (Table 2) and acquired an umbrella shape (Figure 3B and 3D).

Variable-temperature magnetic susceptibility measurements for complexes **1** and **2** were performed using a SQUID magnetometer at an external magnetic field of 1 T. An inverse magnetic behavior between the complexes has been observed (Figure 4). While complex **1** was a paramagnetic material, complex **2** was a diamagnetic material with magnetic moment

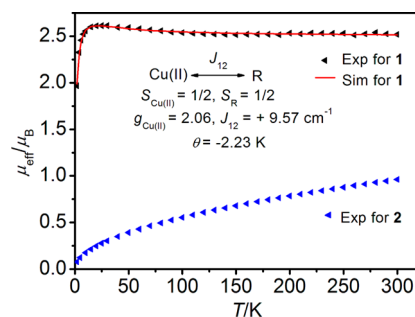


Figure 4. μ_{eff} vs T plots for complexes **1** and **2**.

(μ_{eff}) = $0.96 \mu_{\text{B}}$ at 300 K, which reached $0.08 \mu_{\text{B}}$ at 2 K. In the case of complex **1**, at 300 K μ_{eff} was $2.52 \mu_{\text{B}}$, which represented a system comprised of a noninteracting Cu(II) [$g_{\text{Cu(II)}} = 2.10$] and π -radical ($g_{\text{R}} = 2.00$) units. Upon cooling, the μ_{eff} value remained almost constant up to 75 K and then increased to $\mu_{\text{eff}} = 2.58 \mu_{\text{B}}$ at 20 K. The μ_{eff} of **1** again decreased and reached $\mu_{\text{eff}} = 1.97 \mu_{\text{B}}$ at 2 K. The increase in μ_{eff} with a decrease in temperature indicated a ferromagnetic coupling between the $d_{x^2-y^2}$ magnetic orbital of the Cu(II) ion and the p_z orbital of coordinated π -radical. The further decrease in μ_{eff} was presumably due to intermolecular antiferromagnetic coupling. This experimental result was simulated using the following parameters: $g_{\text{Cu(II)}} = 2.06$, $g_{\text{R}} = 2.00$, $J = +9.57 \text{ cm}^{-1}$, and $\theta = -2.23 \text{ K}$.

The angle between the N1–Cu–O1 and the N2–Cu–O2 planes has been defined as the twist angle. It was previously reported that a ferromagnetic coupling would persist between the $d_{x^2-y^2}$ magnetic orbital of the Cu(II) ion and the p_z orbital of the coordinated π -radical for the twist angle ranging between 0° and $\sim 20^\circ$. Beyond that an antiferromagnetic coupling between the orbitals would predominate.⁸ Herein, the twist angle was $\sim 10^\circ$ in complex **2**, while that was 21° in complex **1** (Table 2). Therefore, a ferromagnetic coupling was expected in complex **2**, while the coupling would be antiferromagnetic in complex **1**. However, an opposite effect was observed. Although a higher torsion angle has been observed in complex **2** compared to complex **1** (Table 2, Figure 3C and 3D), the angle difference was not sufficient enough to invert the coupling fashion. Hence, for complexes **1** and **2** the coupling between the spins was not determined by either the twist angle or the torsion angle. The higher bent angle (Figure 5, Table 2, $\sim 11^\circ$)

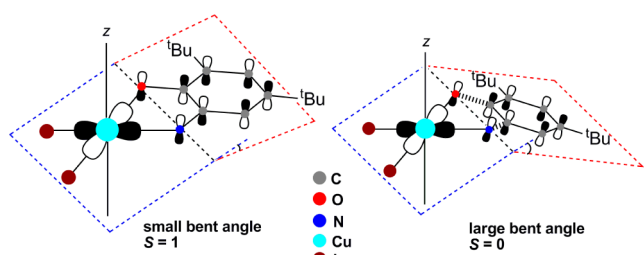


Figure 5. Bent angle-dependent arrangements of magnetic orbitals.

and the higher virtual angle (vide supra, $\sim 20^\circ$) in complex **2** compared to complex **1** were the probable reasons for the antiferromagnetic coupling in complex **2**. Due to the change in hybridization of the C13 atom from sp^3 to sp^2 (vide supra) the flexibility in the six-membered Cu–N1–C7–C12–C13–N2 ring decreases. This decrease promoted a nonplanar geometry in the coordinated ligand backbone in complex **2**.

The electronic absorption spectra for complexes **1** and **2** are shown in Figure 6. The spectra were dominated mainly by intense charge-transfer transitions. A comparatively moderate band at $\lambda_{\text{max}} = 970 \text{ nm}$ ($\epsilon = 1800 \text{ M}^{-1} \text{ cm}^{-1}$) for **1** and at $\lambda_{\text{max}} = 1000 \text{ nm}$ ($\epsilon = 800 \text{ M}^{-1} \text{ cm}^{-1}$) for **2** possibly appeared because of ligand (phenolate, salicylidene) to ligand (iminobenzosemiquinone, amidophenolate) intervalence charge transfer (IVCT). The intraligand charge transfer due to the presence of π -radical^{11a,15} appeared at $\lambda_{\text{max}} = 845 \text{ nm}$ ($\epsilon = 2900 \text{ M}^{-1} \text{ cm}^{-1}$) for **1** and 800 nm ($\epsilon = 1950 \text{ M}^{-1} \text{ cm}^{-1}$) for **2**. The intense absorption band at $\lambda_{\text{max}} = 540 \text{ nm}$ ($\epsilon = 3050 \text{ M}^{-1} \text{ cm}^{-1}$) in the electronic spectrum of **1** was due to ligand [phenolate] to metal

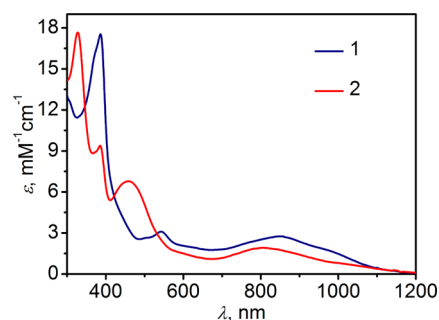


Figure 6. UV-vis/NIR spectra of **1** and **2** measured at 25°C in CH_2Cl_2 solution.

[Cu(II)] charge transfer (LMCT) [vide infra].^{2f,11c} The electronic spectrum of **2** showed a broad band at $\lambda_{\text{max}} = 460 \text{ nm}$ ($\epsilon = 6800 \text{ M}^{-1} \text{ cm}^{-1}$), which has been found to be a ligand to ligand charge transfer (LLCT) [vide infra]. The other intense bands in the UV region were attributed to a π system transition within the iminobenzosemiquinone moiety.⁸

The electrochemical behavior of the complexes was studied by cyclic voltammetry. Cyclic voltammograms (CVs) of complexes **1** and **2** have been recorded in CH_2Cl_2 solutions containing 0.10 M [$(n\text{Bu})_4\text{N}$]ClO₄ as supporting electrolyte at a glassy carbon working electrode, a platinum wire counter electrode, and a Ag/AgNO₃ reference electrode. Ferrocene was used as an internal standard, and potentials are referenced versus the ferrocenium/ferrocene couple (Fc^+/Fc).

Both complexes showed two reversible oxidations and one reversible reduction wave (Figure 7), and the results are given

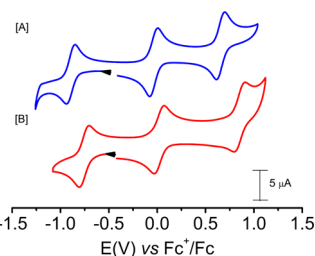


Figure 7. CV curves of **1** [A] and **2** [B] recorded in CH_2Cl_2 at ambient temperature with a scan rate of 100 mV/s . Potentials were referenced to the Fc/Fc^+ couple.

Table 3. Voltammetric Redox Processes for Complexes **1** and **2**

complex	$E^{0,a} \text{ V } (\Delta E_p, \text{ mV})$		
	$E_{1/2}^{\text{red1}}$	$E_{1/2}^{\text{ox1}}$	$E_{1/2}^{\text{ox2}}$
1	$-0.900 (85)$	$-0.040 (80)$	$0.660 (80)$
2	$-0.760 (100)$	$0.022 (95)$	$0.852 (100)$

^a E^0 values recorded at scan rates of 100 mV/s and referenced to the Fc/Fc^+ couple.

in Table 3. CVs measurements at different scan rates (50 , 100 , and 200 mV/s) did not show any shift in the position of the peaks. Note that although the potential difference between the complexes for the first oxidation process ($E_{1/2}^{\text{ox1}}$) was only 62 mV ($\{E_{1/2}^{\text{ox1}}\} = -0.040 \text{ V}$ [**1**]; 0.022 V [**2**]), a significant potential difference for the second oxidation process ($E_{1/2}^{\text{ox2}}$)

[0.660 V (1), 0.852 V (2)] as well as for the sole reduction process ($E_{1/2}^{\text{red1}}$) [−0.900 V (1), −0.760 V (2)] were observed. The calculated $\Delta E_{1/2}^{\text{ox}}$ values using $\Delta E_{1/2}^{\text{ox}} = E_{1/2}^{\text{ox2}} - E_{1/2}^{\text{ox1}}$ were 700 and 830 mV for complexes 1 and 2, respectively. This 130 mV higher $\Delta E_{1/2}^{\text{ox}}$ in the case of complex 2 indicated a higher extent of electrochemical communication between the two redox-active sites in the complex compared to that in complex 1. A significant interaction between the Cu(II) and the π -radical in complex 2 could be argued as the promoter for this higher extent of communication.

From X-ray crystallographic analysis (vide supra) it was evident that both complexes acquired one coordinated π -radical, which was the only site that could be reduced feasibly at the observed potential. Therefore, the reduction process was assigned to reduction of the π -radical (iminobenzosemiquinone) to the corresponding phenolate (amidophenolate) unit. The first oxidation process for both complexes could be either oxidation of a π -radical that would lead to formation of an iminobenzoquinone from the iminobenzosemiquinone unit or oxidation of the Cu(II)-coordinated phenolate unit that would generate a Cu(II)–phenoxyl radical. In order to assign the actual oxidation site, 1 equiv of AgSbF_6 was added in a CH_2Cl_2 solution of each complex. The consequent UV–vis/NIR spectral changes for the complexes have been recorded and are depicted in Figure 8.^{16a} No vanishing of the broad

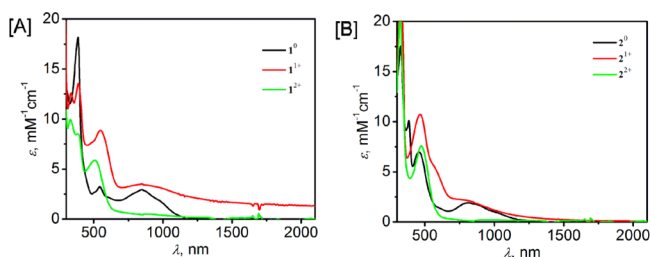


Figure 8. Absorption spectra of the complexes: (A) 1 (black), 1^{1+} (red), and 1^{2+} (green); (B) 2 (black), 2^{1+} (red), and 2^{2+} (green).

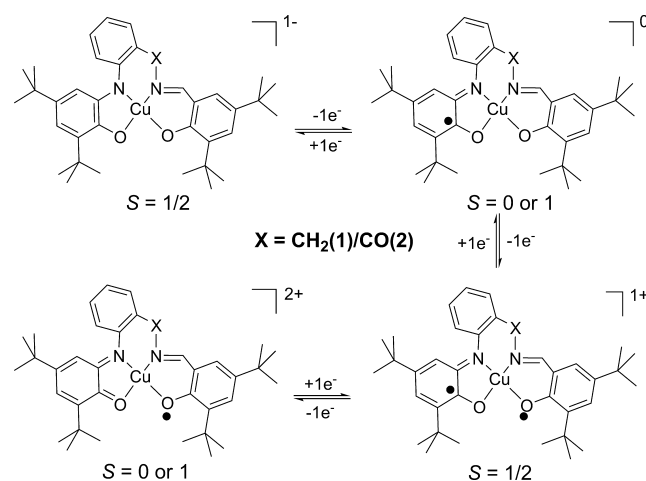
absorption band centered at 845 [1] and 800 [2] nm discarded the possibility of oxidation of the π -radical unit to the corresponding quinone unit. Furthermore, the increase of band intensity at ~ 850 ($\epsilon = 3300 \text{ M}^{-1} \text{ cm}^{-1}$) and 550 ($\epsilon = 8450 \text{ M}^{-1} \text{ cm}^{-1}$) nm for complex [1]¹⁺ and ~ 810 ($\epsilon = 2750 \text{ M}^{-1} \text{ cm}^{-1}$), 570 ($\epsilon = 7000 \text{ M}^{-1} \text{ cm}^{-1}$), and 470 ($\epsilon = 13450 \text{ M}^{-1} \text{ cm}^{-1}$) nm for complex [2]¹⁺ confirmed formation of the phenoxyl radical.^{3d,e,j,8} The second oxidation of 1 and 2 was carried out by addition of 2 equiv of cerium ammonium nitrate (CAN) in a 1:1 CH_2Cl_2 : CH_3CN solvent mixture. In this oxidation, the absorption band at 845 [1] and 800 [2] nm almost vanished (Figure 8, Table 4). This indicated oxidation of the π -radical (iminobenzosemiquinone) moiety to the corre-

Table 4. Absorption Data of the Complexes

complex	λ_{max} nm (ϵ , $\text{M}^{-1} \text{ cm}^{-1}$)
1^0	970 (1800), 845 (2900), 540 (3050), 383 (18 150)
1^{1+}	850 (3300), 550 (8450), 387 (13 400), 335 (12 600)
1^{2+}	510 (5900), 387 (8450), 330 (9900)
2^0	1000 (800), 800 (1950), 460 (6800)
2^{1+}	810 (2200), 570 (5450), 466 (10 750)
2^{2+}	470 (7600)

sponding iminobenzoquinone moiety in both complexes. The presence of the strong band at 510 [1^{2+}] and 470 [2^{2+}] nm further supported formation of a quinone moiety (π to π^* charge transfer).^{16b} Note, the Cu(II)-coordinated phenoxyl radical is also known to exhibit π to π^* charge transfer in the 400–500 nm region.^{16c,d} Therefore, the band could be a combination of quinone and phenoxyl π to π^* charge transfers. Thus, the overall electrochemical behavior of 1 and 2 can be summarized as shown in Scheme 3.

Scheme 3



In order to understand the electronic spin state and coupling nature among the three $S = 1/2$ spins [one Cu(II) and two radicals] of [1]⁺ and [2]⁺ species, X-band EPR measurements were performed. In both cases, four-line signals appeared (Figure 9), which confirmed that the locus of the unpaired electron was on the Cu(II) center ($^{63}\text{Cu} I = 3/2$). Hence, a higher extent of an antiferromagnetic coupling between the two radical centers than that of the Cu(II) and a radical center could be argued. Simulation to the experimental results provided the following parameters: $g_1 = 2.100\{[1]^+\}$, $2.100\{[2]^+\}$; $g_2 =$

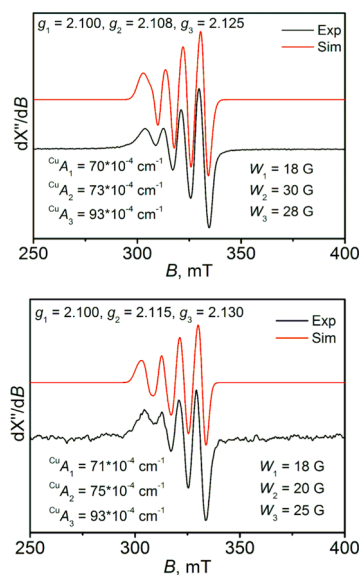


Figure 9. Experimental and simulated X-band EPR spectra of [1]¹⁺ (top) and [2]¹⁺ (bottom). Experiments were performed at RT.

2.108{[1]⁺}, 2.115{[2]⁺}; $g_3 = 2.125\{[1]^+\}, 2.130\{[2]^+\}$, $g_{av} = 2.111\{[1]^+\}, 2.115\{[2]^+\}$, ${}^{Cu}(A_1, A_2, A_3) = (70, 73, 93) \times 10^{-4} \text{ cm}^{-1}\{[1]^+\}$ (71, 75, 93) $\times 10^{-4} \text{ cm}^{-1}\{[2]^+\}$. Using the relation $g_{av} = 1/3(g_{||} + 2g_{\perp})$ it was found that $g_{||} = 2.125$ and $g_{\perp} = 2.104$ for [1]⁺ and $g_{||} = 2.130$ and $g_{\perp} = 2.107$ for [2]⁺. The $g_{||} > g_{\perp}$ indicated that the unpaired electron resided on the $d_{x^2-y^2}$ magnetic orbital of Cu(II) in [1]⁺ and [2]⁺.^{11c}

DFT-Based Computational Study. The structures of both complexes were optimized at the B3LYP^{19,20} level using all-electron 6-31G(d,p) basis sets. The optimized geometries of the complexes are presented in Figure 10. Selected computed bond distances and bond angles along with their experimental counterparts are included in Table S1.

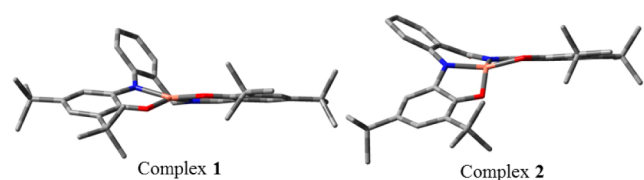


Figure 10. Optimized structures of the complexes at the B3LYP/6-31G(d,p) level in tube form. Hydrogen atoms are removed for clarity.

Complex 1 retained its square planar geometry to a significant extent with a small structural deformation. However, in complex 2 the structural geometry was distorted toward tetrahedral shape. It was observed from the FMO pictures of complex 1 that the $d_{x^2-y^2}$ orbital of the central Cu(II) was perpendicular to the plane containing ligand π orbitals (Figure S6). This particular orbital orientation minimized the spatial overlap between the orthogonal $d_{x^2-y^2}$ orbital of Cu(II) and the coordinated π orbital of the ligand radical and, consequently, favored the same spin alignment and ferromagnetic coupling in complex 1. However, complex 2, owing to a larger virtual angle between planes A and C, generated a favorable situation for the orbital overlap between the $d_{x^2-y^2}$ orbital of Cu(II) and the ligand π orbitals (Figure S7). Accordingly, the higher probability of orbital mixing in complex 2 led to an energetically favorable spin pairing between the unpaired electrons. This is the origin of the diamagnetism in complex 2.¹⁷

A detailed natural population analysis (NPA) was also performed to understand the overall electronic environment around the Cu(II) center in both complexes (Table S2). The splitting of d orbitals and corresponding NAO (natural atomic orbital) occupancies for both complexes are also listed in Table S2. In complex 2 the d orbitals of the central Cu(II) atom were found to be higher in energy than those in complex 1. This implied relatively strong interactions between the Cu(II) center and the coordinating ligand. Because of the interactions, the orbital degeneracy was significantly disturbed in complex 2.

The magnetostructural correlations in square planar Cu(II) complexes at the molecular level were investigated using hybrid DFT-based calculations. The spin density plot for complex 1 is reported in Figure 11. From the spin density plot it was observed that in complex 1 the unpaired electrons having the same spin orientations were mainly localized on both the central Cu(II) atom and the π -radical containing five-membered chelate ring. Thus, a theoretical study predicted the same spin alignment and a higher possibility of ferromagnetic coupling between the unpaired electrons that were present in complex 1. The energetic stability of the

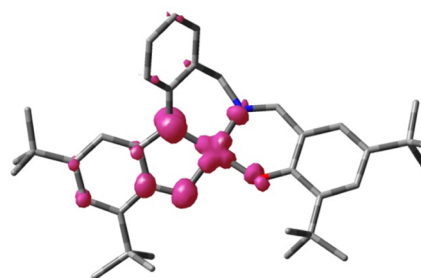


Figure 11. Pictorial representation of spin density map (isodensity 0.003 electron/Bohr³) for complex 1. The violet color regions represent the location of α spin density. Hydrogen atoms are omitted for clarity.

systems (high spin or low spin) also provided useful insights to determine the spin states for unpaired electrons. Computed optimized energy values for both complexes at different states are given in Table S3. It was found that the triplet state of complex 1 was stabilized by -8.49 kcal/mol relative to the singlet ground state, whereas in the broken-symmetry solution for complex 1 (spin contamination, $\langle S^2 \rangle = 2.00011$) the singlet state was destabilized by 3.77 kcal/mol with respect to the triplet state. Thus, the possibility of the energetically favorable triplet electronic state with probable ferromagnetic coupling between the unpaired electrons in complex 1 was evident. In addition, the computed FMO pictures (Figure S6) for complex 1 revealed that the SOMO (for both α and β) was primarily located on the ligand side and there was no such mixing of metal d and ligand π orbitals. Therefore, the orbital symmetry would be retained and more ferromagnetic coupling would prevail between the unpaired electrons.

One of the convincing ways to model the antiferromagnetic coupling is the broken-symmetry SCF solution (as implemented in Gaussian09).¹⁸ The fragmentation patterns considered for this particular discussion for both complexes are reported in Figure S8. It is observed that the broken-symmetry solution, with reasonably acceptable spin contamination, $\langle S^2 \rangle = 0.028862$, for complex 2 has stabilized the antiferromagnetically coupled state by -2.12 kcal/mol relative to the singlet ground state. On the other hand, the triplet state for complex 2 was destabilized by 7.77 kcal/mol with respect to the broken-symmetry singlet state. This indicates the higher probability of an energetically favorable antiferromagnetically coupled state for the unpaired electrons in complex 2. The pictorial representation of the spin density map for complex 2 is given in Figure 12. The locations of opposite spin densities on the

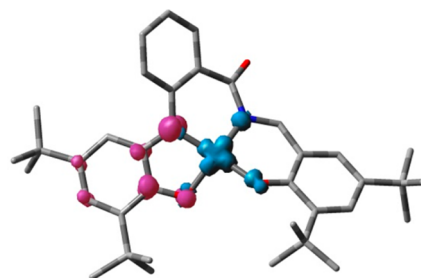


Figure 12. Pictorial representation of the spin density map for complex 2 obtained from broken-symmetry calculation. The violet-colored regions represent the location of the α spin, and blue represents the β spin. Hydrogen atoms are omitted for clarity.

metal (violet) and the ligand (blue) support the probable antiferromagnetic coupling pattern of the unpaired electrons. It is worth noting that the relatively large amount of structural distortion led to a greater overlap of the Cu 3d orbitals with the π orbitals of the coordinated ligand. This was further evident from the FMO pictures of complex **2** (Figure S7) along with their calculated individual AOs contribution. As a consequence of the higher degree of orbital mixing, the triplet state gets destabilized due to the Pauli repulsion between like spin pairs.⁸ Furthermore, the significantly high HOMO–LUMO energy gap (1.98 eV) for complex **2** supports the antiferromagnetic coupling pattern of the unpaired electrons. Herein, it is worth mentioning that the DFT-based findings on the magnetic behavior of both complexes were consistent with the experimental results.

To find the sites of oxidations we optimized the geometries of the monopositive and dipositive species for both complexes. The energy values are given in Table S4. For comparison of atomic charges (Mulliken) as well as bond distances of the coordination sphere the optimized geometries of the most stable spin states of the neutral as well oxidized species were chosen. The charge values and bond distances are shown in Tables S5 and S6, respectively. It is clear from Table S5 that the loss of an electron from the Cu atom after the oxidations was not significant; rather, the generated positive charge was delocalized over the coordinating ligand backbone. After one-electron oxidation, the changes in bond distances (Table S6, Figure S9) were found more in the redox-active aminophenol moiety rather than the expected redox-inactive salicylidene unit. This unexpected trend in the calculated bond distances and atomic charges might be attributed to the inherent limitation in our calculations, which were performed in the gas phase. Furthermore, the higher electron loss of the aminophenol moiety instead of expected redox-inactive salicylidene in the first oxidation step could also be attributed to exclusion of counterion (SbF_6^-) in the structure chosen for optimization. Recently, Asami et al.¹⁹ have also shown that the localized phenoxyl radical observed experimentally in the solid state cannot be reproduced in the theoretical calculation, particularly when the counterion is not considered.

Excited State Calculation. To simulate the experimental UV–vis/NIR spectra of the complexes, solvent-phase TD-DFT calculations are performed at the B3LYP/6-31G(d,p)/IEF-PCM (solvent model) level with DCM as solvent for both complexes. The corresponding FMO pictures generated from TD-DFT calculation are reported in Figure S10. The vertical excitation energies calculated for the lowest lying singlet and triplet states for studied complexes are reported in Table 5. The strong absorption at 524 nm ($f = 0.19$) in complex **1** corresponded to a combination of SOMO–3 to SUMO and SOMO–2 to SUMO, interligand charge-transfer (ILCT) and ligand to metal charge-transfer (LMCT) transitions. This particular transition was well correlated to the experimentally observed peak at 540 nm. Additionally, in complex **1**, the two relatively weak transitions at 842 ($f = 0.03$) and 977 nm ($f = 0.01$) correspond to π to π^* intraligand charge-transfer (ILCT) and interligand charge-transfer (LLCT/IVCT) transitions and correlated to the observed peaks at 845 and 970 nm. In complex **2** the calculated transition appeared at 450 nm ($f = 0.22$) that resulted from strong ligand-centric $\pi(\text{L})$ to $\pi^*(\text{L})$ electronic excitations. This particular transition correlated well with the experimentally observed peak at 460 nm. Hence, the peak at 460 nm can be assigned as π to π^* intraligand charge

Table 5. TD-DFT-Computed Transitions Correspond to the Most Intense Peaks in the Experimental UV–vis/NIR Spectrum of the Complexes at the B3LYP/6-31G(d,p) Level

state	ΔE , eV (nm)	f^a	C.I. contribution
complex 1			
T1	1.27 (977)	0.01	SOMO \rightarrow SUMO (58%)
T2	1.47 (842)	0.03	SOMO–1 \rightarrow SUMO (97%) SOMO \rightarrow SUMO (2%)
S4	2.37 (524)	0.19	SOMO \rightarrow SUMO (8%) SOMO–2 \rightarrow SUMO (23%) SOMO–3 \rightarrow SUMO (56%) SOMO–4 \rightarrow SUMO (13%)
complex 2			
T1	1.34 (930)	0.0025	HOMO–1 \rightarrow LUMO (85%) HOMO \rightarrow LUMO (4%)
S2	1.64 (757)	0.02	HOMO \rightarrow LUMO (9%) HOMO–1 \rightarrow LUMO (83%) HOMO–2 \rightarrow LUMO (4%)
S7	2.76 (450)	0.22	HOMO \rightarrow LUMO (5%) HOMO–3 \rightarrow LUMO (12%) HOMO–4 \rightarrow LUMO (57%) HOMO–1 \rightarrow LUMO+1 (6%)

^aTD-DFT oscillator strength.

transfer. From the theoretical calculation relatively weak π to π^* ligand to ligand charge-transfer (LLCT) transitions were found at 757 ($f = 0.02$) and 930 nm ($f = 0.003$). Hence, the observed peaks at 800 and 1000 nm that appeared in the UV–vis/NIR spectrum of complex **2** could be assigned as LLCT transitions.

Subsequently, the electron density difference was computed between the ground (S_0) and the lowest identified singlet (S_1) and triplet (T_1) excited states. It is more logical to identify the locations of the electron density shift during electronic excitations using the density difference plot as reported in Figure S11. It was observed from the density difference plot that the singlet excitations (S_0 to S_1) are primarily dominated by LMCT ($p\pi$ to $d\pi$) types of electronic transitions where d orbitals of the central Cu atom were significant in both complexes. However, for complexes **1** and **2** a π to π^* intraligand electronic transition was predominant in triplet excitations (S_0 to T_1).

CONCLUSION

Employing ligand $\text{H}_3\text{Sami}^{\text{Mixed}(\text{tBu})}$, which composed of one noninnocent aminophenol and one innocent salicylidene compartments, complex **1** has been synthesized. The complex undergoes ligand-centered oxidation at the benzyl $-\text{CH}_2$ position under air in solution, thus forming complex **2**. X-ray single-crystal analysis indicates that both complexes are monoradical-coordinated mononuclear Cu(II). The overall geometry of complex **1** is almost planar, while complex **2** is umbrella shaped. Although a higher twist angle is found in complex **1**, ferromagnetic coupling is realized in the complex. Therefore, the twist angle based nonorthogonal relation between the $d_{x^2-y^2}$ magnetic orbital of the Cu(II) ion and the coordinated π -radical is no longer in the present system. Rather, a bent angle has been found as the suitable explanation for the ferromagnetic coupling in **1** and antiferromagnetic coupling in **2**. The DFT-based theoretical calculation also supports the observed magnetic behavior. Chemical oxidation along with cyclic voltammetric studies indicate that oxidation of phenolate to phenoxyl radical is more preferable compared to

oxidation of iminobenzosemiquinone to iminobenzoquinone. This suggests that in both complexes the coordinated π -radical is highly stable. Although complex **1** is more planar than complex **2**, a higher extent of electrochemical communication between the redox sites (phenoxy and π -radical) is observed in complex **2** because of the strong communication between the central Cu(II) and the π -radical centers.

EXPERIMENTAL SECTION

Materials. All chemicals and solvents were obtained from commercial sources and used as supplied unless noted otherwise. 3,5-Di-*tert*-butylcatechol, 2-aminobenzonitrile, 3,5-di-*tert*-butyl salicylaldehyde, and LiAlH₄ were purchased from Sigma-Aldrich. Solvents were obtained from Merck (India). THF was dried before used. Mass spectra were measured in HPLC-grade acetonitrile solution.

Physical Methods. X-ray crystallographic data for **1** were collected using a Bruker SMART APEX-II CCD diffractometer equipped with a fine focus 1.75 kW sealed tube Mo K α radiation ($\lambda = 0.71073$ Å) at 296(2) K with increasing ω (width of 0.3° per frame) at a scan speed of 3 s/frame. A single crystal of **2** was measured on a Super Nova, single source at offset, Eos diffractometer. The structure was solved with the Superflip structure solution program using charge flipping and refined by direct methods using SHELXS-97 and with full-matrix least-squares on F^2 using SHELXL-97. In both cases all nonhydrogen atoms were refined anisotropically. IR spectra were recorded on a PerkinElmer Instrument at normal temperature with a KBr pellet by grinding the sample with KBr (IR grade). UV–vis spectra were recorded on a PerkinElmer Lambda 750 UV/vis/NIR spectrometer by preparing a known concentration of the samples in HPLC-grade CH₂Cl₂ at room temperature using a cuvette of 1 cm width. Mass spectral (MS) data were obtained from a quadrupole time-of-flight (QTOF) MS spectrometer (Waters, model Q-ToF Premier), and peaks are given in m/z (% of basis peak). Variable-temperature magnetic susceptibility measurements were performed using a superconducting quantum interference device (SQUID) magnetometer at 1 T for both complexes. Simulations of the experimentally obtained magnetic measurements were performed using the *JulX* program developed by Dr. E. Bill.

Computational Details. We performed DFT-level calculations on complexes **1** and **2** to understand the magnetic behavior along with the experimental UV–vis/NIR spectrum of the complexes. The structures are optimized at the B3LYP^{20,21} level using all-electron 6-31+G(d,p) basis sets for all atoms including Cu. The ferromagnetic and antiferromagnetic coupling patterns of the unpaired electrons in complexes **1** and **2** are modeled through spin-restricted singlet, broken-symmetry singlet, and spin-unrestricted triplet state. Excited state calculations (TD-DFT study) are also performed at the B3LYP/6-31+G(d,p) level. In the excited state calculations the explicit solvent effect is considered through the IEF-PCM model²² for DCM solvent. The ferromagnetic and antiferromagnetic coupling patterns of the unpaired electrons in complexes **1** and **2** are modeled through spin-restricted singlet, broken-symmetry singlet, and spin-unrestricted triplet state. The Gaussian09 software package¹⁸ was used in the entire calculation.

Synthesis of [C₂₁H₃₀N₂O], H₄L^{CH₂NH₂}, and [C₂₈H₃₄N₂O₂], H₃L^{Mixed(H)}}.} The synthetic procedures for both ligands H₄L^{CH₂NH₂}} and H₃L^{Mixed(H)}} were reported previously.¹³

Synthesis of [C₃₆H₄₇CuN₂O₂], **1.** A solution of H₄L^{CH₂NH₂}} (0.326 g, 1 mmol) and 3,5-di-*tert*-butylsalicylaldehyde (0.234 g, 1 mmol) in CH₃CN (15 mL) was heated at reflux for 3 h. After cooling to room temperature, CuCl₂·2H₂O (0.172 g, 1 mmol) and Et₃N (0.2 mL) were added sequentially. Then the resulting reaction mixture was stirred for 6 h at room temperature (30 °C). A brown precipitate of **1** appeared. The precipitate was filtered and washed thoroughly with CH₃CN. Yield: 0.300 g, 50%.

The resulting residue was recrystallized from a 4:1 CH₂Cl₂:CH₃CN solvent mixture by the slow solvent evaporation technique. This provided two distinct crystalline solids, which were separated manually. The block-shaped large crystalline solid was isolated as a

Table 6. Crystallographic Data and Structure Refinement Parameters for **1 and **2****

	1	2
empirical formula	C ₃₆ H ₄₇ CuN ₂ O ₂	C ₃₆ H ₄₅ CuN ₂ O ₃
fw	603.30	617.28
cryst habit, color	block/brown	needle/brown
cryst size (mm ³)	0.52 × 0.40 × 0.26	0.30 × 0.18 × 0.15
temperature, <i>T</i> (K)	296(2)	296(2)
wavelength, λ (Å)	0.71073	0.71073
cryst syst	monoclinic	orthorhombic
space group	C2/c	P2 ₁ 2 ₁ 2 ₁
unit cell dimens	<i>a</i> = 28.094(4) Å <i>b</i> = 3.778(2) Å <i>c</i> = 19.626(3) Å $\alpha = \gamma = 90^\circ$, $\beta = 114.714(7)^\circ$	<i>a</i> = 6.3536(4) Å <i>b</i> = 19.2147(13) Å <i>c</i> = 27.2831(14) Å $\alpha = \beta = \gamma = 90^\circ$
volume, <i>V</i> (Å ³)	6901.1(17)	3330.8(4)
<i>Z</i>	8	4
calcd density (mg·m ⁻³)	1.161	1.231
Absorption coefficient, μ (mm ⁻¹)	0.664	0.692
<i>F</i> (000)	2576	1312
θ range for data collection	1.60–26.00°	2.99–25.00°
limiting indices	−34 ≤ <i>h</i> ≤ 34, −14 ≤ <i>k</i> ≤ 16, −24 ≤ <i>l</i> ≤ 24	−4 ≤ <i>h</i> ≤ 7, −22 ≤ <i>k</i> ≤ 16, −32 ≤ <i>l</i> ≤ 24
no. of reflns collected/unique	44 784/6598 [<i>R</i> (int) = 0.0440]	9285/5479 [<i>R</i> (int) = 0.0646]
completeness to θ	97.2% ($\theta = 26.00^\circ$)	99.7% ($\theta = 25.00^\circ$)
max and min transmission	0.841 and 0.734	0.901 and 0.861
refinement method	SHELXL-97 (Sheldrick, 1997)	SHELXL-97 (Sheldrick, 1997)
data/restraints/parameters	6598/0/382	5479/0/391
goodness-of-fit on F^2	1.134	1.070
final <i>R</i> indices [<i>I</i> > 2 σ (<i>I</i>)]	<i>R</i> 1 = 0.0393, <i>wR</i> 2 = 0.0944	<i>R</i> 1 = 0.0654, <i>wR</i> 2 = 0.1240
<i>R</i> indices (all data)	<i>R</i> 1 = 0.0685, <i>wR</i> 2 = 0.1043	<i>R</i> 1 = 0.0850, <i>wR</i> 2 = 0.1338
largest diff. peak and hole	0.285 and −0.283 e·Å ⁻³	0.411 and −0.374 e·Å ⁻³

major product. Yield: 0.240 g, 40%. The minor product was complex **2**. FTIR (KBr pellet, cm⁻¹): 2959, 2903, 2862, 1619, 1583, 1530, 1479, 1438, 1429, 1390, 1353, 1329, 1256, 1200, 1168, 912, 875, 840, 752, 502. ESI-MS (CH₃CN) m/z for [C₃₆H₄₇CuN₂O₂]⁺: calcd, 602.29; found, 602.53. Anal. Calcd for C₃₆H₄₇CuN₂O₂: C, 71.67; H, 7.85; N, 4.64. Found: C, 71.64; H, 7.65; N, 4.53.

Synthesis of [C₃₆H₄₅CuN₂O₃], **2.** Recrystallization of complex **1** (0.300 g, 0.5 mmol) from a 5:1 CH₂Cl₂:CH₃CN solvent mixture provided complex **2** as a needle-shaped microcrystalline solid in 5 days. The procedure was followed twice. The isolated crystalline solid was suitable for single-crystal X-ray diffraction study. Yield: 0.125 g, 40%. FTIR (KBr pellet, cm⁻¹): 3441, 2960, 2948, 2903, 2863, 1657, 1621, 1557, 1528, 1474, 1438, 1349, 1326, 1288, 1217, 1195, 1173, 1159, 1111, 1024, 1002, 913, 767, 753. ESI-MS (CH₃CN) m/z for [C₃₆H₄₅CuN₂O₃]⁺: calcd, 616.28; found, 616.54. Anal. Calcd for C₃₆H₄₅CuN₂O₃: C, 70.05; H, 7.35; N, 4.54. Found: C, 70.32; H, 7.14; N, 4.34.

ASSOCIATED CONTENT

Supporting Information

The Supporting Information is available free of charge on the ACS Publications website at DOI: 10.1021/acs.inorgchem.5b01257.

Infrared, mass spectra, DTF calculation data for complexes **1** and **2** (PDF) (CIF)

(CIF)

AUTHOR INFORMATION

Corresponding Author

*E-mail: cmukherjee@iitg.ernet.in.

Notes

The authors declare no competing financial interest.

ACKNOWLEDGMENTS

This project was funded by CSIR [01(2817/14/EMR-II)]. S.G. thanks CSIR and UGC (India) for his fellowship. A.S. is grateful to the UGC-BSR, Government of India, for granting him research fellowships. R.K.R. acknowledges the DST (Project ref. No. SB/S1/PC-067/2013), Government of India, and Department of Chemistry, BITS PILANI, Pilani, for financial and computational support.

REFERENCES

- (1) (a) MacMillan, F.; Kannt, A.; Behr, J.; Prinsner, T.; Michel, H. *Biochemistry* **1999**, *38*, 9179–9184. (b) Bleifuss, G.; Kolberg, M.; Pötsch, S.; Hofbauer, W.; Bittl, R.; Lubitz, W.; Gräslund, A.; Lassmann, G.; Lendzian, F. *Biochemistry* **2001**, *40*, 15362–15368. (c) Nugent, J. H. A.; Ball, R. J.; Evans, M. C. W. *Biochim. Biophys. Acta, Bioenerg.* **2004**, *1655*, 217–221. (d) Schünemann, V.; Lendzian, F.; Jung, C.; Contzen, J.; Barra, A.-L.; Sligar, S. G.; Trautwein, A. X. *J. Biol. Chem.* **2004**, *279*, 10919–10930. (e) Reece, S. Y.; Seyedsayamdost, M. R.; Stubbe, J.; Nocera, D. G. *J. Am. Chem. Soc.* **2007**, *129*, 13828–13830. (f) Whittaker, J. W. In *Metalloenzymes Involving Amino Acid Residue and Related Radicals*; Sigel, H., Sigel, A., Eds.; Marcel Dekker: New York, 1994. (g) Knowles, P. F.; Ito, N. In *Perspectives in Bio-inorganic Chemistry*; Jai Press Ltd.: London, 1994. (h) Rogers, M. S.; Dooley, D. M. *Curr. Opin. Chem. Biol.* **2003**, *7*, 189–196. (i) Rittle, J.; Green, M. T. *Science* **2010**, *330*, 933–937.
- (2) Some examples are as follows: (a) Poddel'sky, A. I.; Cherkasov, V. K.; Abakumov, G. A. *Coord. Chem. Rev.* **2009**, *253*, 291–324. (b) Mondal, M. K.; Biswas, A. K.; Ganguly, B.; Mukherjee, C. *Dalton Trans.* **2015**, *44*, 9375–9381. (c) Chaudhuri, P.; Wieghardt, K. Phenoxyl Radical Complexes. In *Progress in Inorganic Chemistry*; Wiley: Hoboken, NJ, 2001. (d) Chaudhuri, P.; Wieghardt, K.; Weyhermüller, T.; Paine, T. K.; Mukherjee, S.; Mukherjee, C. *Biol. Chem.* **2005**, *386*, 1023–1033. (e) Rakshit, R.; Ghorai, S.; Biswas, S.; Mukherjee, C. *Inorg. Chem.* **2014**, *53*, 3333–3337. (f) Mukherjee, C.; Pieper, U.; Bothe, E.; Bachler, V.; Bill, E.; Weyhermüller, T.; Chaudhuri, P. *Inorg. Chem.* **2008**, *47*, 8943–8956. (g) Pierpont, C. G.; Lange, C. W. The Chemistry of Transition-Metal Complexes Containing Catechol and Semiquinone Ligands. In *Progress in Inorganic Chemistry*; Karlin, K. D., Ed.; Wiley: Hoboken, NJ, 1994. (h) Blackmore, K. J.; Sly, M. B.; Haneline, M. R.; Ziller, J. W.; Heyduk, A. F. *Inorg. Chem.* **2008**, *47*, 10522–10532. (i) Rajput, A.; Sharma, A. K.; Barman, S. K.; Koley, D.; Steinert, M.; Mukherjee, R. *Inorg. Chem.* **2014**, *53*, 36–48. (j) Das, D.; Scherer, T. M.; Das, A.; Mondal, T. K.; Mobin, S. M.; Fiedler, J.; Luis Priego, J.; Jimenez-Aparicio, R.; Kaim, W.; Lahiri, G. K. *Dalton Trans.* **2012**, *41*, 11675–11683. (k) Smith, A. L.; Hardcastle, K. I.; Soper, J. D. *J. Am. Chem. Soc.* **2010**, *132*, 14358–14360. (l) Lyaskovskyy, V.; de Bruin, B. *ACS Catal.* **2012**, *2*, 270–279. (m) Luca, O. R.; Crabtree, R. H. *Chem. Soc. Rev.* **2013**, *42*, 1440–1459. (n) Kaim, W. *Eur. J. Inorg. Chem.* **2012**, *2012*, 343–348. (o) Hindson, K.; de Bruin, B. *Eur. J. Inorg. Chem.* **2012**, *2012*, 340–342. (p) Itoh, S.; Taki, M.; Takayama, S.; Nagatomo, S.; Kitagawa, T.; Sakurada, N.; Arakawa, R.; Fukuzumi, S. *Angew. Chem., Int. Ed.* **1999**, *38*, 2774–2776. (q) Ghorai, S.; Mukherjee, C. *Chem. Commun.* **2012**, *48*, 10180–10182. (r) Bag, S. S.; Ghorai, S.; Mukherjee, C. *RSC Adv.* **2013**, *3*, 5374–5377. (s) Rakshit, R.; Ghorai, S.; Sarmah, A.; Roy, R. K.; Mukherjee, C. *Dalton Trans.* **2015**, *44*, 3724–3727. (t) Benisvy, L.; Blake, A. J.; Collision, D.; Davies, E. S.; Garner, C. D.; McInnes, E. J. L.; McMaster, J.; Whittaker, G.; Wilson, C. *Chem. Commun.* **2001**, 1824–1825. (u) Chirik, P. J.; Wieghardt, K. *Science* **2010**, *327*, 794–795. (v) Mukherjee, C.; Weyhermüller, T.; Bothe, E.; Chaudhuri, P. *Inorg. Chem.* **2008**, *47*, 11620–11632. (w) Mukherjee, C.; Weyhermüller, T.; Bothe, E.; Rentschler, E.; Chaudhuri, P. *Inorg. Chem.* **2007**, *46*, 9895–9905. (x) Thompson, J. S.; Calabrese, J. C. *Inorg. Chem.* **1985**, *24*, 3167–3171.
- (3) (a) Jeschke, G. *Biochim. Biophys. Acta, Bioenerg.* **2005**, *1707*, 91–102. (b) Verma, P.; Pratt, R. C.; Storr, T.; Wasinger, E. C.; Stack, T. D. P. *Proc. Natl. Acad. Sci. U. S. A.* **2011**, *108*, 18600–18605. (c) Chaudhuri, P.; Hess, M.; Weyhermüller, T.; Wieghardt, K. *Angew. Chem., Int. Ed.* **1999**, *38*, 1095–1098. (d) Müller, J.; Weyhermüller, T.; Bill, E.; Hildebrandt, P.; Ould-Moussa, L.; Glaser, T.; Wieghardt, K. *Angew. Chem., Int. Ed.* **1998**, *37*, 616–619. (e) Mijovilovich, A.; Hamman, S.; Thomas, F.; de Groot, F. M. F.; Weckhuysen, B. M. *Phys. Chem. Chem. Phys.* **2011**, *13*, 5600–5604. (f) Thomas, F. *Eur. J. Inorg. Chem.* **2007**, *2007*, 2379–2404. (g) Orio, M.; Jarjayes, O.; Kanso, H.; Philouze, C.; Neese, F.; Thomas, F. *Angew. Chem., Int. Ed.* **2010**, *49*, 4989–4992. (h) Halfen, J. A.; Young, V. G., Jr.; Tolman, W. B. *Angew. Chem., Int. Ed. Engl.* **1996**, *35*, 1687–1690. (i) Wang, Y.; DuBois, J. L.; Hedman, B.; Hodgson, K. O.; Stack, T. D. P. *Science* **1998**, *279*, 537–540. (j) Itoh, S.; Takayama, S.; Arakawa, R.; Furuta, A.; Komatsu, M.; Ishida, A.; Takamuku, S.; Fukuzumi, S. *Inorg. Chem.* **1997**, *36*, 1407–1416. (k) Zurita, D.; Gautier-Luneau, I.; Menage, S.; Pierre, J.-L.; Saint-Aman, E. *JBIC, J. Biol. Inorg. Chem.* **1997**, *2*, 46–55. (l) Berreau, L. M.; Mahapatra, S.; Halfen, J. A.; Houser, R. P.; Young, V. G., Jr.; Tolman, W. B. *Angew. Chem., Int. Ed.* **1999**, *38*, 207–210. (m) Shimazaki, Y.; Takani, M.; Yamauchi, O. *Dalton Trans.* **2009**, 7854–7869. (n) Benisvy, L.; Blake, A. J.; Collision, D.; Davies, E. S.; Garner, C. D.; McInnes, E. J. L.; McMaster, J.; Whittaker, G.; Wilson, C. *Dalton Trans.* **2003**, 1975–1985. (o) Ruf, M.; Noll, B. C.; Groner, M. D.; Yee, G. T.; Pierpont, C. G. *Inorg. Chem.* **1997**, *36*, 4860–4865.
- (4) (a) Whittaker, J. W. In *Bioinorganic Chemistry of Copper*; Karlin, K. D., Tyeklar, Z., Eds.; Chapman & Hall, Inc.: New York, 1993. (b) Whittaker, J. W. *Chem. Rev.* **2003**, *103*, 2347–2363. (c) Thomas, F. In *Stable Radicals: Fundamentals and Applied Aspects of Odd-Electron Compounds*; Hicks, R., Ed.; Wiley: Hoboken, NJ, 2010. (d) Rokhsana, D.; Howells, A. E.; Dooley, D. M.; Szilagy, R. K. *Inorg. Chem.* **2012**, *51*, 3513–3524. (e) Ito, N.; Phillips, S. E. V.; Yadav, K. D. S.; Knowles, P. F. *J. Mol. Biol.* **1994**, *238*, 704–814.
- (5) (a) Storr, T.; Verma, P.; Pratt, R. C.; Wasinger, E. C.; Shimazaki, Y.; Stack, T. D. P. *J. Am. Chem. Soc.* **2008**, *130*, 15448–15459. (b) Rotthaus, O.; Jarjayes, O.; Thomas, F.; Philouze, C.; Saint-Aman, E.; Pierre, J.-L. *Dalton Trans.* **2007**, 889–895. (c) Wang, Y.; Stack, T. D. P. *J. Am. Chem. Soc.* **1996**, *118*, 13097–13098. (d) Saint-Aman, E.; Menage, S.; Pierre, J.-L.; Degrançq, E.; Gellou, G. *New J. Chem.* **1998**, *22*, 393–394.
- (6) Chaudhuri, P.; Hess, M.; Müller, J.; Hildenbrand, K.; Bill, E.; Weyhermüller, T.; Wieghardt, K. *J. Am. Chem. Soc.* **1999**, *121*, 9599–9610.
- (7) (a) Shimazaki, Y. *PATAI's Chemistry of Functional Groups*; John Wiley & Sons, Ltd.: New York, 2012. (b) Shimazaki, Y.; Yamauchi, O. *Indian J. Chem.* **2011**, *50A*, 383–394. (c) Thomas, F.; Jarjayes, O.; Duboc, C.; Philouze, C.; Saint-Aman, E.; Pierre, J.-L. *Dalton Trans.* **2004**, 2662–2669. (d) Balaghi, S. E.; Safaei, E.; Chiang, L.; Wong, E. W. Y.; Savard, D.; Clarke, R. M.; Storr, T. *Dalton Trans.* **2013**, *42*, 6829–6839.
- (8) Verma, P.; Weir, J.; Mirica, L.; Stack, T. D. P. *Inorg. Chem.* **2011**, *50*, 9816–9825.
- (9) (a) Kahn, O.; Prins, R.; Reedijk, J.; Thompson, J. S. *Inorg. Chem.* **1987**, *26*, 3557–3561. (b) Debnath, R. K.; Kalita, A.; Kumar, P.; Mondal, B.; Ganguli, J. N. *Polyhedron* **2013**, *51*, 222–227.
- (10) (a) Koth, D.; Gottschaldt, M.; Görls, H.; Pohle, K. *Beilstein J. Org. Chem.* **2006**, *2* (17), 1–5. (b) Gaballa, A. S. *J. Chem. Pharm. Res.* **2013**, *5*, 206–217. (c) Kuźniarska-Biernacka, I.; Carvalho, M. A.; Rasmussen, S. B.; Bañares, M. A.; Biernacki, K.; Magalhães, A. L.; Rolo, A. G.; Fonseca, A. M.; Neves, I. C. *Eur. J. Inorg. Chem.* **2013**, *2013*, 5408–5417. (d) Sabarinathan, S.; Vasuki, G.; Rao, P. S. *Eur. J. Chem.* **2010**, *1*, 360–367.

- (11) (a) Chaudhuri, P.; Verani, C. N.; Bill, E.; Bothe, E.; Weyhermüller, T.; Wieghardt, K. *J. Am. Chem. Soc.* **2001**, *123*, 2213–2223. (b) Ye, S.; Sarkar, B.; Lissner, F.; Schleid, T.; van Slageren, J.; Fiedler, J.; Kaim, W. *Angew. Chem., Int. Ed.* **2005**, *44*, 2103–2106. (c) Ghorai, S.; Mukherjee, C. *Chem. - Asian J.* **2014**, *9*, 3518–3524.
- (12) Addison, A.; Rao, T.; Reedijk, J.; van Rijn, J.; Verschoor, G. J. *Chem. Soc., Dalton Trans.* **1984**, 1349–1356.
- (13) Ghorai, S.; Mukherjee, C. *Dalton Trans.* **2014**, *43*, 394–397.
- (14) (a) Mukherjee, C.; Stämmler, A.; Bögge, H.; Glaser, T. *Inorg. Chem.* **2009**, *48*, 9476–9484. (b) Mukherjee, C.; Stämmler, A.; Bögge, H.; Glaser, T. *Chem. - Eur. J.* **2010**, *16*, 10137–10149. (c) Glaser, T.; Heidemeier, M.; Fröhlich, R.; Hildebrandt, P.; Bothe, E.; Bill, E. *Inorg. Chem.* **2005**, *44*, 5467–5482. (d) Rotthaus, O.; Jarjayes, O.; Thomas, F.; Philouze, C.; Perez Del Valle, C.; Saint-Aman, E.; Pierre, J. L. *Chem. - Eur. J.* **2006**, *12*, 2293–2302.
- (15) Franks, M.; Gadzhieva, A.; Ghandhi, L.; Murrell, D.; Blake, A. J.; Davies, E. S.; Lewis, W.; Moro, F.; McMaster, J.; Schröder, M. *Inorg. Chem.* **2013**, *52*, 660–670.
- (16) (a) In order to understand the completeness of the oxidation reaction as well as the stability of the corresponding one-electron- and two-electron-oxidized species, time-dependent spectral changes were recorded. No spectral change was observed up to 1 h (examination period). (b) Mukherjee, C.; Weyhermüller, T.; Bothe, E.; Chaudhuri, P. *Inorg. Chem.* **2008**, *47*, 2740–2746. (c) Zats, G. M.; Arora, H.; Lavi, R.; Yufit, D.; Benisvy, L. *Dalton Trans.* **2011**, *40*, 10889–10896. (d) Shimazaki, Y.; Yamauchi, O. *Indian J. Chem. Sec. A* **2011**, *50*, 383–394.
- (17) (a) Dei, A.; Gatteschi, D.; Pardi, L.; Russo, U. *Inorg. Chem.* **1991**, *30*, 2589–2594. (b) Pierpont, C. G.; Attia, A. S. *Collect. Czech. Chem. Commun.* **2001**, *66*, 33–51.
- (18) Frisch, M. J. et al. *GAUSSIAN 09*, Revision C.01; Gaussian, Inc.: Wallingford, CT, 2009.
- (19) Asami, K.; Takashina, A.; Kobayashi, M.; Iwatsuki, S.; Yajima, T.; Kochem, A.; van Gastel, M.; Tani, F.; Kohzuma, T.; Thomas, F.; Shimazaki, T. *Dalton Trans.* **2014**, *43*, 2283–2293.
- (20) Becke, A. D. *J. Chem. Phys.* **1993**, *98*, 5648–5652.
- (21) Lee, C. T.; Yang, W. T.; Parr, R. G. *Phys. Rev. B: Condens. Matter Mater. Phys.* **1988**, *37*, 785–789.
- (22) Cancès, E.; Mennucci, B.; Tomasi, J. *J. Chem. Phys.* **1997**, *107*, 3032–3041.